



**Universiteit  
Leiden**  
The Netherlands

## **Spectroscopy and nuclear dynamics of starburst galaxies**

Vermaas, L.

### **Citation**

Vermaas, L. (2012, January 11). *Spectroscopy and nuclear dynamics of starburst galaxies*. Retrieved from <https://hdl.handle.net/1887/18332>

Version: Corrected Publisher's Version

License: [Licence agreement concerning inclusion of doctoral thesis in the Institutional Repository of the University of Leiden](#)

Downloaded from: <https://hdl.handle.net/1887/18332>

**Note:** To cite this publication please use the final published version (if applicable).

# Nuclear gas dynamics of Ultraluminous Infrared Galaxies



L. Vermaas, N. Neumayer and P. P. van der Werf

## Abstract

We present high resolution near-infrared integral field spectroscopy of a sample of ultraluminous infrared galaxies (ULIRGs). We derive velocity fields for the nebular emission lines and model these using sets of tilted rotating rings. The resulting rotation curves are analysed with mass models consisting of a combination of a purely stellar Hernquist bulge and an exponential disk, which is mostly or completely gaseous. This analysis results in dynamical masses, stellar masses, and stellar  $K$ -band mass to light ratios, within the region observed, for all our targets. The most important source of uncertainty in the analysis is the inclination of the gas disks. We find that for 50% of our targets, the derived stellar masses match the independently determined values based on the stellar dynamics (derived in Chapter 4). These objects display gas velocity fields that are well represented by the tilted ring models. In the other 50% of the cases discrepancies are found between the masses derived using gas dynamics and stellar dynamics, and we attribute these mostly to bulk gas motions that are not well represented using a set of tilted rings. We use our results to investigate the location of our targets with respect to the fundamental plane of dynamically hot stellar systems, and find an offset which can be attributed fully to the  $M/L$  ratios of our targets, which are lower than those of quiescent more evolved ellipticals. Passive evolution in the light profile will eventually bring these objects on the fundamental plane in the region of intermediate mass and luminosity ellipticals (and not of giant, massive ellipticals), unless further dynamical evolution would increase the effective radii by factor of about three.

## 5.1 Introduction

Ultraluminous infrared galaxies (ULIRGs) are spectacular systems with infrared luminosities  $L_{\text{IR}} \geq 10^{12} L_{\odot}$ . Nearly all are strongly interacting merger systems with a large amount of molecular gas, while most of the interstellar matter is concentrated in the inner regions of these objects, with extreme nuclear starbursts. The energy source is a combination of starburst and an active galactic nucleus (AGN), in varying proportion, as derived from spectroscopy and imaging at wavelengths from radio to X-rays. ULIRGs have a range in infrared spectral energy distributions, which is often expressed in the ratio of flux in the  $25 \mu\text{m}$  and the  $60 \mu\text{m}$  bands: “cool” ULIRGs have a typical ratio  $f_{25}/f_{60} \leq 0.10$ , whereas for “warm” ULIRGs  $f_{25}/f_{60} > 0.2$ . Warm ULIRGs have compact, bright nuclei compared to cool ULIRGs.

The AGN-starburst connection has become a central issue with the discovery of the relation between stellar velocity dispersion and mass of the central black hole in spheroidal stellar systems (Magorrian et al. 1998, Ferrarese & Merritt 2000, Gebhardt et al. 2000). Given that elliptical galaxies are mainly old, this relation has to be put in place at their formation history. Since ULIRGs form stars at prodigious rates,  $10^2 - 10^3 M_{\odot} \text{yr}^{-1}$ , and often host an AGN as well, they may be regarded as local analogs to forming spheroids. These points have been emphasised in extensive studies by Genzel et al. (2001) and Tacconi et al. (2002). While these studies indicate that local ULIRGs evolve into intermediate mass rather than giant ellipticals, they are still the best available local laboratories for studying the processes occurring in more luminous high- $z$  objects such as the sub-mm galaxies, which may be the sites of the coeval explosive buildup of stellar mass and a supermassive black hole.

A conceptually simple mechanism for establishing a relation between stellar mass and black hole mass is based on feedback from the AGN terminating star formation. Sanders et al. (1988) argue that ULIRGs are dust-obscured precursors of QSOs. On this evolutionary path, the AGN disperses the dust and gas, shifting the bulk of energy toward shorter wavelengths, eventually becoming an optically bright QSO. In the context of the coeval buildup of stellar mass and black hole mass, the dispersal of dust and gas would also terminate star formation, and thus provides a possible mechanism for establishing a relation between black hole mass and stellar mass: once the black hole becomes so massive that its feedback on the environment disperses the gas, it shuts down star formation and the stellar mass is fixed. The dispersal of the gas also limits further growth of the black hole. The stellar mass is then given by the integral of star formation over time during the ULIRG phase, the black hole mass by the integral of accretion rate over time.

The accumulation of gas, followed by star formation and subsequent dispersal of the gas thus forms a key process in the evolution of ULIRGs. While the stellar components of the original galaxies are in a slow process of merging by dynamical friction, the gas components merge much faster because the gas can dissipate mechanical energy. The gas thus flows toward the centre of the potential well on a short timescale, where it forms a disk or ring. CO interferometry (e.g., Downes & Solomon 1998) shows that such structures are ubiquitous in local ULIRGs, and that gas moves on circular orbits in an ordered velocity field characterised by a rising rotation curve in the inner part which flattens at a radius of about 0.5 kpc or smaller. A theory by Elmegreen (1994) is that the molecular disk is initially stable against

star formation because of the high shear in the nuclear region, which keeps the Toomre  $Q$ -parameter high. The continuing buildup of surface density in the disk makes it eventually Toomre-unstable and an explosive phase of star formation follows, because the gas density must be very high before the shear can be overcome. This process is expected to destroy the disk and disperse the gas, and a forming AGN, if present, becomes visible.

Near infrared observations show that  $\text{H}_2$  emission is an excellent tracer of these disks. The bright emission of the vibrational  $\text{H}_2$   $2.12\ \mu\text{m}$  line is a general characteristic of ULIRGs (Goldader et al. 1995), while this line is much weaker (relative to total IR luminosity) in less luminous starbursts. A detailed study of the nucleus of Cen A with SINFONI data by Neumayer et al. (2007) shows that the  $\text{H}_2$  is the best gas tracer of the potential in galactic nuclei. The  $\text{H}_2$  emission has a fairly complex flux distribution but its velocity field is characteristic of a rotating disk. This disk can be modelled by a set of tilted rings, which fits the data extremely well, in spite of the complex flux distribution. In contrast, the other emission lines ([FeII], Br $\gamma$ , [SiVI]) are increasingly affected by non-gravitational motions. The fact that  $\text{H}_2$  traces the potential well closely is confirmed by the agreement in black hole masses as derived from the  $\text{H}_2$  data and the stellar kinematics using CO bandhead from the same dataset (Cappellari et al. 2009). Neumayer et al. show that any residual unresolved gas velocity dispersion in the disk can be included using a small pressure term in the dynamical equations.

If ULIRGs indeed evolve into elliptical galaxies, they should also show the characteristic scaling relations of elliptical galaxies, in particular the so-called Fundamental Plane (FP), which relates the effective radius  $R_{\text{eff}}$ , the average surface brightness within  $R_{\text{eff}}$ , and the central velocity dispersion of an elliptical galaxy. On the other hand, the location of a galaxy with respect to the FP depends on its mass to light ratio ( $M/L$ ), and an important evolving young stellar population will have a different  $M/L$  than a quiescent elliptical galaxy.

In this paper we present our SINFONI, AO-assisted near infrared integral field spectroscopic observations of a small sample of ULIRGs with colours ranging from “cool” to “warm”. While the stellar dynamics are analysed in Chapter 4, here we focus on the dynamical properties of the nuclear gas disks determined from the same data sets. We derive rotation curves, and present dynamical models for these. Finally, we discuss the implications of our results for the understanding of the evolution of these systems.

## 5.2 Observations and data reduction

Six objects were selected from the IRAS Revised Bright Galaxy Sample (Sanders et al. 2003). For qualification as an ULIRG,  $L_{\text{ir}} \geq 10^{12}$  and our targets meet this requirement within the errors of measurement for  $L_{\text{ir}}$ . We used a redshift criterion  $z \leq 0.12$ , in order to have enough spatial resolution and to be able to detect stellar CO-bandheads. The sample spans a range in infrared colours, in order to have a “sequence” from cool to warm ULIRGs (QSOs), albeit with very limited statistics. The infrared colour is determined by the ratio of flux in the  $25\ \mu\text{m}$  band and the  $60\ \mu\text{m}$  band ( $f_{25}/f_{60}$ ;  $< 0.2$  qualifies as ‘cool’ and  $> 0.2$  qualifies as ‘warm’). The analysis of Arp 220, has been discussed in Chapter 3, and is here included for comparison.

**Table 5.1** – Observed sources

Name	$z$	$\log(L_{\text{ir}}/L_{\odot})$	$f_{25}/f_{60}$	kpc $''$
IRAS 01388-4618	0.090289	12.03	0.12	1.79
IRAS F05189-2524	0.042563	12.09	0.26	0.84
IRAS F09111-1007	0.054141	11.95	0.11	1.07
IRAS F17208-0014	0.042810	12.33	0.05	0.86
IRAS F20551-4250	0.042996	11.98	0.15	0.86
Arp 220	0.018126	12.21	0.06	0.36

<sup>a</sup> The analysis of Arp 220, with a double nucleus in the  $K$ -band, is described in Chapter 3 and is included for comparison reasons.

The objects were observed with SINFONI, the Spectrograph for INtegral Field Observations in the Near Infrared (1.1 - 2.45  $\mu\text{m}$ ), which is installed on UT4 of the VLT (Eisenhauer et al. 2003, Bonnet et al. 2004), the Laser Guide Star facility was used for Adaptive Optics. Since no bright nearby reference stars were available, the optical host galaxies were used for tip-tilt sensing. Since this procedure is not optimal (but no better option was available), Strehl ratios and angular resolution were somewhat reduced with respect to the ideal case. The intermediate platescale was used, with a field of view of 3 $''$ x3 $''$  onto 64x64 spatial pixels. Each of these pixels is projected onto 2218 spectral elements in the  $K$ -band, with a central wavelength of 2.2 $\mu\text{m}$ . This results in spatial pixels with a resolution of 0.05 $''$ x0.10 $''$ , and a spectral resolution  $\lambda/\Delta\lambda$  of 4000.

For the pointings, an ABA'-nodding mode was used, i.e. object-sky-object with equal integration times of 900 s, with the A' frame slightly shifted with respect to the A frame. The total (on-source) integration time was 6x900 s, or 75 minutes in most cases. The observations of IRAS 01388-0014, IRAS 05189-2524 and IRAS 09111-1007 were carried out on December 29 and 30, 2007, with average visual seeing of 0.8 $''$ . The observations of IRAS 17208-0014 and IRAS 20551-4250 were carried out on July 18 and 19 of 2009 with an average visual seeing of 0.7 $''$ . Achieved Strehl ratios were in the order of 0.20-0.30.

The data were reduced with the SINFONI pipeline, which was developed by ESO and the Max-Planck-Institut für extraterrestrische Physik. The default procedure included corrections for pixel non-linearity, distortion and wavelength calibration.

For both flux calibration and telluric feature removal, a standard star was observed with the same setup as was used for the science frames, typically an early type star containing few stellar lines in the NIR. After reduction, the average stellar spectrum was extracted and the stellar lines were removed (Br  $\gamma$ ). Finally, each spectrum of the object frame was divided by this extracted spectrum.

In the case of IRAS 01388-4618, IRAS 05189-2524 and IRAS 09111-1007, the PSF was 0.24 $''$ (FWHM) as determined from the [SiVI] line map of IRAS 09111-1007, which is as-

sumed to originate from a point-source. For IRAS 17208-0014 and IRAS 20551-4250, the PSF-size was determined from observations of QSO Mrk 1014, in the same night, with the same instrumental setup and was measured to be  $0.2''$  (FWHM).

Our datasets provide measurements of gas kinematics and stellar kinematics in the same dataset, but in this chapter we focus on only the gas kinematics, and describe the stellar kinematics separately in Chapter 4.

## 5.3 Results and analysis

### 5.3.1 Spectra and images

Fig. 5.1 shows the nuclear spectra of the observed ULIRGs. The Pa  $\alpha$  and Br  $\gamma$  recombination lines are generally strong in ULIRGs that are in their “cool” phase. Also luminous H<sub>2</sub> is a general characteristic of ULIRGs. Stellar CO absorption bands are detected in some ULIRGs, dependent on redshift; an analysis of stellar kinematics is carried out in Chapter 4.

The emission lines Pa  $\alpha$ , Br  $\gamma$ , and the H<sub>2</sub> vibrational lines were fitted with single Gaussians in each pixel. The resulting maps of the H<sub>2</sub> and Pa  $\alpha$  line emission, as well as the *K*-band continuum are shown per galaxy in Figs. 5.2-5.11 (a), (c) and (e). In most objects, Pa  $\alpha$  as well as H<sub>2</sub> are peaking at the nucleus position. In some cases, the Pa  $\alpha$  map shows a distorted morphology, most likely a result of the merging process. The same figures show the velocity field of H<sub>2</sub> (b) and Pa  $\alpha$  (d) and the velocity dispersion of either H<sub>2</sub> or Pa  $\alpha$  (f).

### 5.3.2 Tilted ring fitting

The H<sub>2</sub> and Pa  $\alpha$  velocity fields were fitted with a set of tilted rings, using the IDL-based code Kinemetry (Krajnović et al. 2006). The kinematic centre position was fixed, tilted rings were fitted at increasing radii ( $r$ ), with position angle (PA) as free parameter and the flattening ( $q = b/a = \cos i$ ) fixed, or free within a very small range. The inclination was determined by either (literature) measurements of molecular (CO) gas, or using axis ratios from high resolution radio continuum or the *K*-band image, in that order of preference, as specified in Table 5.2. The fit parameters are also in table 5.2.

The bottom panels of Figs. 5.2-5.11 show the Kinemetry model velocity field from either Pa  $\alpha$  or H<sub>2</sub> (g) and the residual map ( $v_{\text{res}} = v_{\text{orig}} - v_{\text{circ}}$ ) (h). The (symmetric) model rotation curve (inclination-corrected) extracted along the line of nodes (marked by  $\diamond$ ) is for each object presented in a separate figure in the text.

### 5.3.3 Rotation curves, dynamical masses and $M/L_K$

We inserted the inclination corrected gas rotation curve from Pa  $\alpha$ , or H<sub>2</sub> in the case of IRAS 05189-2524, in GIPSY (the Groningen Image Processing SYstem, an interactive software system for the reduction and display of astronomical data) and used the procedure ROTMAS to make a model of the mass. Each rotation curve was fitted with a combination of a

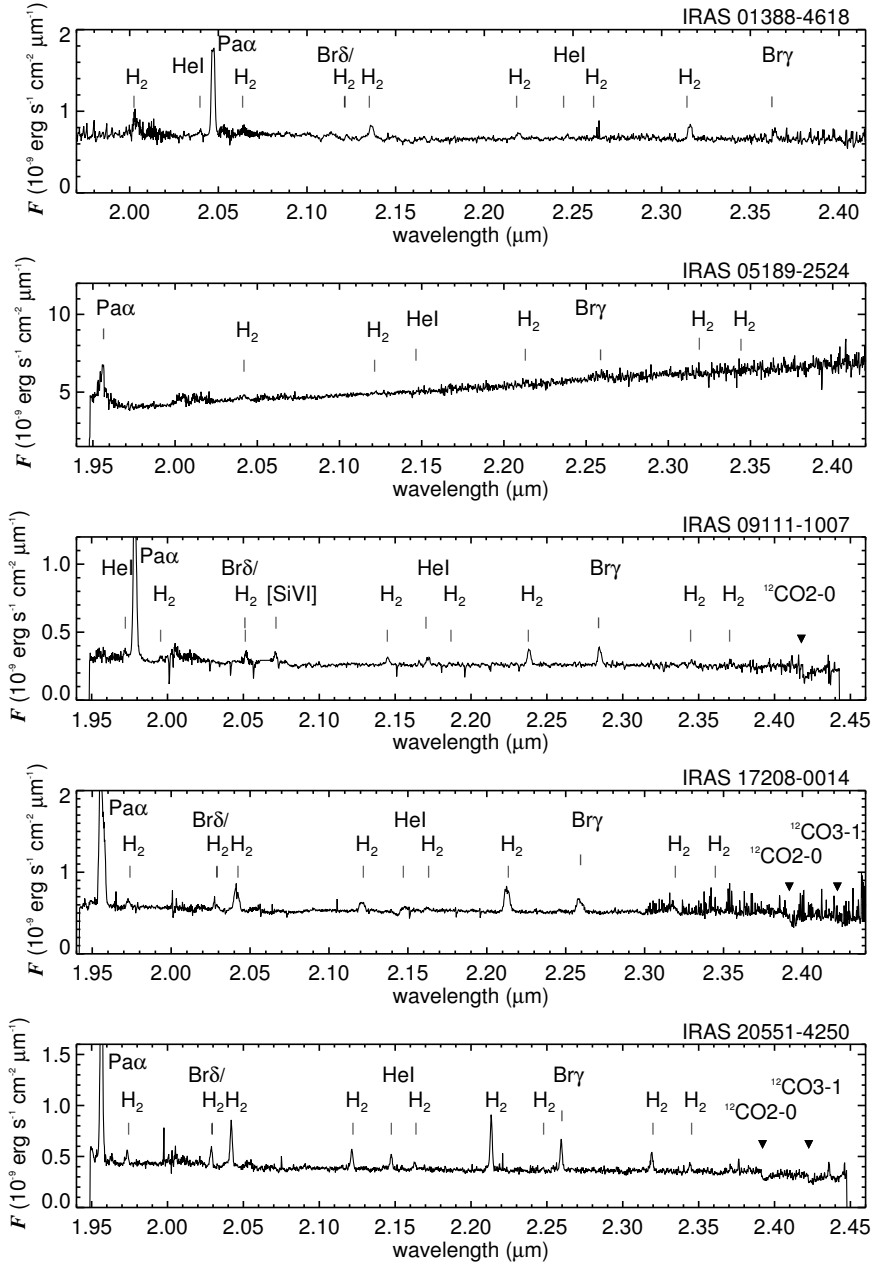


**Figure 5.1** – Integrated K-band spectra of (top to bottom) IRAS 01388-4618, IRAS 05189-2524, IRAS 09111-1007, IRAS 17208-0014, IRAS 20551-4250.

**Table 5.2** – Kinemetry parameters: inclination ( $i$ , fixed in the fit) and its possible range range, position angle (PA) and range (free in the fit), the radius of flattening of the rotation curve ( $R_{\text{flat}}$ ) and the maximum velocity ( $v_{\text{max}}$ ). Results of the GIPSY-fit of the rotation curve with exponential disk and bulge and Hernquist components are also given.

Name	$\langle i \rangle$ ( $^\circ$ )	[range $i$ ] ( $^\circ$ )	$\langle \text{PA} \rangle$ ( $^\circ$ )	[range PA] ( $^\circ$ )	$R_{\text{flat}}$ (kpc)	$v_{\text{max}}$ (km/s)	exponential disk		Hernquist spheroid	
							$h$ (kpc)	$\Sigma_0$ ( $M_\odot \text{pc}^{-2}$ )	$R_{\text{eff}}$ (kpc)	$M_{\text{b,tot}}$ ( $M_\odot$ )
(1)	(2)	(3)	(4)	(5)	(6)	(7)	(8)	(9)	(10)	(11)
IRAS 01388-4618	$30^b$	[22-44]	56	[46-63]	0.7	210	1.1	$2.1 \cdot 10^3$	1.6	$2.0 \cdot 10^{10}$
IRAS F05189-2524 <sup>a</sup>	$22^b$	[4-27]	90	[81-105]	0.18	91	-	-	0.35	$1.1 \cdot 10^9$
IRAS F09111-1007	$38^b$	[35-44]	62	[55-80]	0.74	242	0.5	$4.0 \cdot 10^3$	2.3	$3.4 \cdot 10^{10}$
IRAS F17208-0014	$28^c$	[25-45]	125	[120-129]	0.38	545	0.46	$5.5 \cdot 10^3$	0.54	$6.4 \cdot 10^{10}$
IRAS F20551-4250	$36^b$	[17-25]	40	[35-47]	0.55	118	0.35	$9.0 \cdot 10^2$	1.5	$5.8 \cdot 10^9$
Arp 220	$40^c$	-	40	[32-53]	-	-	0.35	$1.27 \cdot 10^4$	2.5	$5.1 \cdot 10^{10}$

Columns: (2) Mean inclination of the fit.  $i$  is constraint, or free within a very small range. (3) The range of possible inclinations from ellipse-fitting to the SINFONI  $K$ -band flux image. (4) Mean position angle of the fit. PA is a free parameter without constraints. (5) The range of PA-values in the model. (6) Radius where rotation curve becomes flat. (7) Maximum velocity reached in the rotation curve, inclination corrected. (8) Scale height of the exponential disk fit. (9) Surface mass density of the exponential disk fit. (10) Effective radius of the bulge fit. (11) Total mass of the bulge fit.

<sup>a</sup> Only fit with a bulge component.

<sup>b</sup> Inclination derived from  $K$ -band image.

<sup>c</sup> Inclination derived from CO-data (Downes & Solomon 1998).

Hernquist potential (representing a spheroid or bulge component) and an exponential disk, except the curve of IRAS 05189-2524, which was only fitted with a Hernquist potential.

These objects generally have NIR light profiles that obey a De Vaucouleurs  $r^{1/4}$  law (e.g., Scoville et al. 2000), while the gas components have much flatter flux distributions. We therefore take as starting point that the stellar component of the system is represented by the Hernquist bulge in our fit, while the disk in our fit is assumed to represent the gas component. The correctness of this approach can be verified by comparing the resulting disk masses to literature measurements of the gas mass. This procedure results in a stellar bulge, described by the effective (half light or mass) radius  $R_{\text{eff}}$  and a total bulge mass  $M_{\text{b}}$ , and a gas disk with a scale length  $h$  (kpc) and central surface mass density  $\Sigma_0$  ( $M_{\odot} \text{pc}^{-2}$ ).

The inner part of the rotation curve is most likely not suitable for a reliable fit, for several reasons. First, the extinction in the very centre of the nucleus can be very high, even in the near-IR, so the measured flux and shift of the line are in fact averaged values of the visible edges of the nucleus. For this reason, even extinction measurements from near-IR line ratios are lower limits. Second, many objects of this kind have a ring-shape in the very central region (e.g. Downes & Solomon 1998), in which case no gas is present within a certain radius. Finally, even our high resolution data may not sufficiently resolve the kinematic structure of the gas disk in the nucleus, leading to significant beam smearing at small radii. Therefore, in this fitting process, we focus on fitting the shape of the outer part of the rotation curve, which is sensitive to the enclosed mass, as well as the effective radius of the bulge and the scale length of the disk. The largest uncertainty in the determination of the rotation curve is the inclination. While the effect on the height of the curve ( $v_{\text{max}}$ ) can be quite large, especially when close to face-on, the spatial scale (or the (relative) values of  $R_{\text{eff}}$  and  $h$  in the fit) are hardly affected by inclination changes. The mass of both components was then computed within  $R_{\text{out}}$ , which is the physical radius corresponding to the major axis of largest ellipse region fitted by the Kinemetry code. The results are presented in Table 5.3, columns (3)-(5).

For the same region, the  $K$ -band luminosity ( $L_K$ ) was determined and extinction corrected from a pixel-to-pixel derived extinction map from the line ratio  $\text{Pa } \alpha / \text{Br } \gamma$ , which is described in Chapter 4. The (extinction corrected) values of  $L_K$ ,  $M_{\text{dyn}}/L_K$  and  $M_*/L_K$  are stated in columns (7)-(9) of table 5.3, respectively. Here  $L_K$  is the extinction-corrected  $K$ -band luminosity,  $M_{\text{dyn}}$  is the dynamical mass and  $M_*$  is the stellar mass (i.e., the mass of the fitted Hernquist spheroid), all calculated within the radius  $R_{\text{out}}$ . No formal fit errors are given for the derived masses, this is because the dominant error source is the inclination, and the effects of the uncertainty in the inclination are discussed below in Sect. 5.4.2. The relative contributions of the gas and stellar (or disk and bulge) components of the fit may vary, which directly affects the gas fraction  $M_{\text{gas}}/M_{\text{dyn}}$  and  $M_*/L_K$ , while the total dynamical mass is quite insensitive to this.

### 5.3.4 IRAS 01388-4618

This is the most distant ULIRG of the sample, with a redshift of 0.09.  $H_2$  (Fig. 5.2a) shows a regular distribution, similar to the NIR continuum (upper right) which peaks on the same location.  $\text{Pa}\alpha$  (c) is wide-spread and peaks in the centre as well, but shows an asymmetric distribution with a distorted, arc-like shape to the north. The velocity fields from  $H_2$  (b) and  $\text{Pa}\alpha$  (d), however, are aligned and show very regular rotation about the centre (NIR-peak). The velocity dispersion (only shown for  $\text{Pa}\alpha$ , f) peaks on the kinematic/NIR centre and is extended perpendicular to the kinematic major axis, most likely as a result of beam smearing.

The Kinemetry model fits the  $\text{Pa}\alpha$  velocity field very well, the residual map shows no structure and has very low values. The resulting rotation curve has a maximum (inclination corrected) value of  $\sim 215$  km/s, it turns over at 0.7 kpc and stays flat at least out to a radius of 2.5 kpc. Because of the flat shape, instead of declining, this curve could not be fitted with a Hernquist potential alone and a substantial exponential disk component is inescapable. The resulting effective radius is 1.6 kpc, while literature ( $H$ -band) values range from 1.0 kpc in Genzel et al. (2001) to 2.16 kpc in Dasyra et al. (2006). The total dynamical mass inside the outer radius reached of 2.4 kpc was calculated to be  $2.21 \cdot 10^{10} M_\odot$ , with a gas fraction of 0.46 on this scale. Unfortunately, in this object no molecular gas measurement is available for checking this number. The disk component is however quite obvious in the  $\text{Pa}\alpha$  image, which is much more extended than the  $K$ -band continuum, and shows a prominent feature that may be interpreted as a spiral arm. Without an independent molecular gas mass measurement we cannot verify whether this disk is indeed mostly gaseous, but  $K$ -band light profile is very well fit by a De Vaucouleurs law (Genzel et al. 2001). We note however that because of the relatively high redshift of this object, the physical field of view is large and the rotation curve was measured out to a larger physical radius than in the other objects, in particular significantly beyond  $R_{\text{eff}}$ . Restricting the calculation to the region within  $R_{\text{eff}}$  would result in a smaller gas/stellar mass ratio, since the fits to the rotation curve (Fig. 5.3) show that the bulge component is more important in the central part and the gas fraction within the effective radius is smaller. The value of  $M_{\text{dyn}}/L_K$  is  $0.02 M_\odot/L_{K,\odot}$ , and  $M_*/L_K$  is  $0.01 M_\odot/L_{K,\odot}$ .

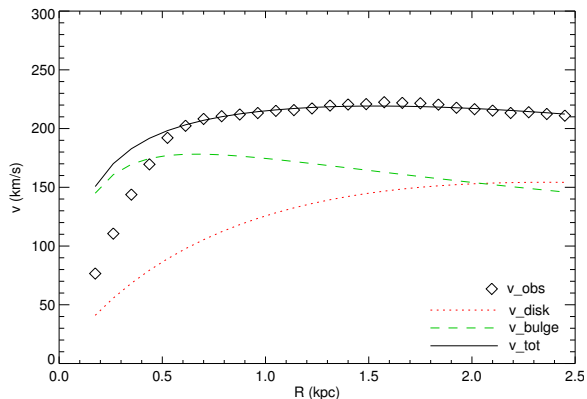
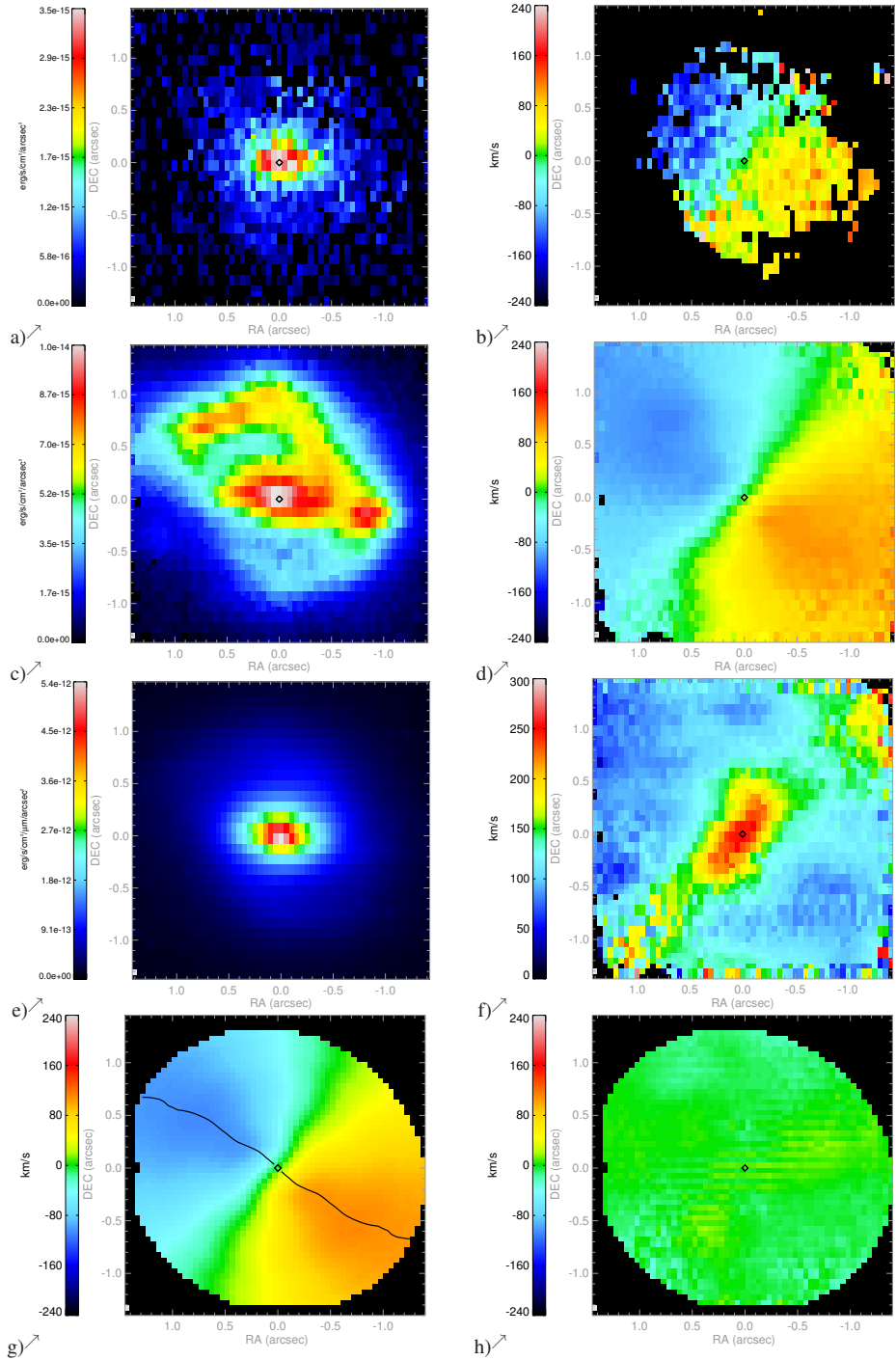


Figure 5.3 – IRAS 01388-4618 gas rotation curve of  $\text{Pa}\alpha$ .



**Figure 5.2** – IRAS 01388-4618 ( $f_{25}/f_{60}=0.12$ ;  $1'' \pm 1.79\text{kpc}$ ): a)  $\text{H}_2$  flux; b)  $\text{H}_2$  velocity; c)  $\text{Pa } \alpha$  flux; d)  $\text{Pa } \alpha$  velocity; e)  $K$ -band continuum; f)  $\text{Pa } \alpha$  velocity dispersion; g) velocity model of  $\text{Pa } \alpha$  and h) residual map. The diamond ( $\diamond$ ) marks the peak of the  $K$ -band continuum, which we use as the kinematic centre by definition.

### 5.3.5 IRAS 05189-2524

This is a well known, well studied object, and with  $f_{25}/f_{60}$  of 0.26, it is the only ULIRG in our sample that qualifies as “warm” ( $f_{25}/f_{60} > 0.2$ ). The spectrum (Fig. 5.1, upper right) shows Pa  $\alpha$ , but not as prominent as in the rest of the sample. Emission lines of excited H<sub>2</sub> are recognised but lines are not prominent in general. This spectrum is the only one with rising  $K$ -band continuum, which indicates the presence of hot dust associated with the AGN. Stellar CO-absorption bands are hardly detected. Figure 5.5 shows a compact source in H<sub>2</sub>, Pa  $\alpha$  and  $K$ . The velocity field is more regular in H<sub>2</sub> (b), than in Pa  $\alpha$  (d) and the velocity dispersion of Pa  $\alpha$  (f) shows a clear peak on the centre location. Since the outer velocity field is noisy, only the very central part of the velocity field is used for modelling, as shown in the bottom panel.

The Pa  $\alpha$  kinematics in this object is strongly affected by the broad line associated with the AGN. The derived velocity field of Pa  $\alpha$  does not match that of H<sub>2</sub>, and is less regular, and based on these arguments, the H<sub>2</sub> velocity map is a better choice for analysing the gravitational dynamics. Because of the compactness of this source, only a small part of the field of view can be used for the Kinometry-fit. Within this small region, however, the residual map is quite smooth, although the low values are not very low compared to the measured velocities. This warm ULIRG has a face-on orientation with literature values for the inclination of  $\sim 20$ – $30^\circ$ . The inclination used in the velocity model is  $22^\circ$ , but we point out that the error margin on this value has large effects on the derived parameters. Since only the inner region of the system can be analysed, no attempt has been made to make a combined bulge+disk fit and the curve is fit with a Hernquist (bulge) potential only. This spheroid has an effective radius of 0.35 kpc and a total mass of  $1.05 \cdot 10^9 M_\odot$ . Dasyra et al. (2006) find an effective radius in  $K$ -band of 0.79 kpc. The dynamic/bulge mass within  $R_{\text{out}}=0.34$  kpc then is  $5.16 \cdot 10^8 M_\odot$ . The stellar mass-to-light ratio  $M_*/L_K$  is  $0.003 M_\odot/L_{K,\odot}$ , which is the same as the value of the  $M_{\text{dyn}}/L_K$  stated in Table 5.3 because only a bulge component was fit to the rotation curve. Besides the extinction correction, a 55% for the AGN component was subtracted in determining  $L_K$ , as described in more detail in Chapter 4.

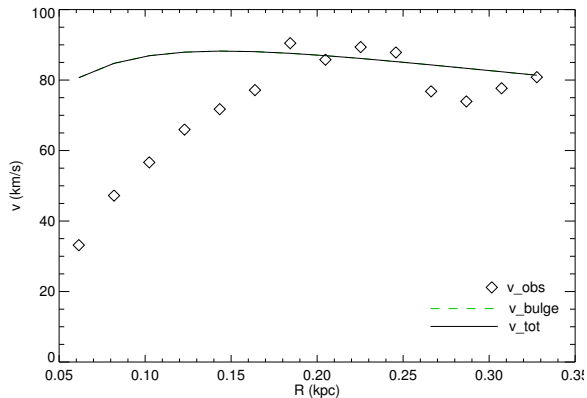
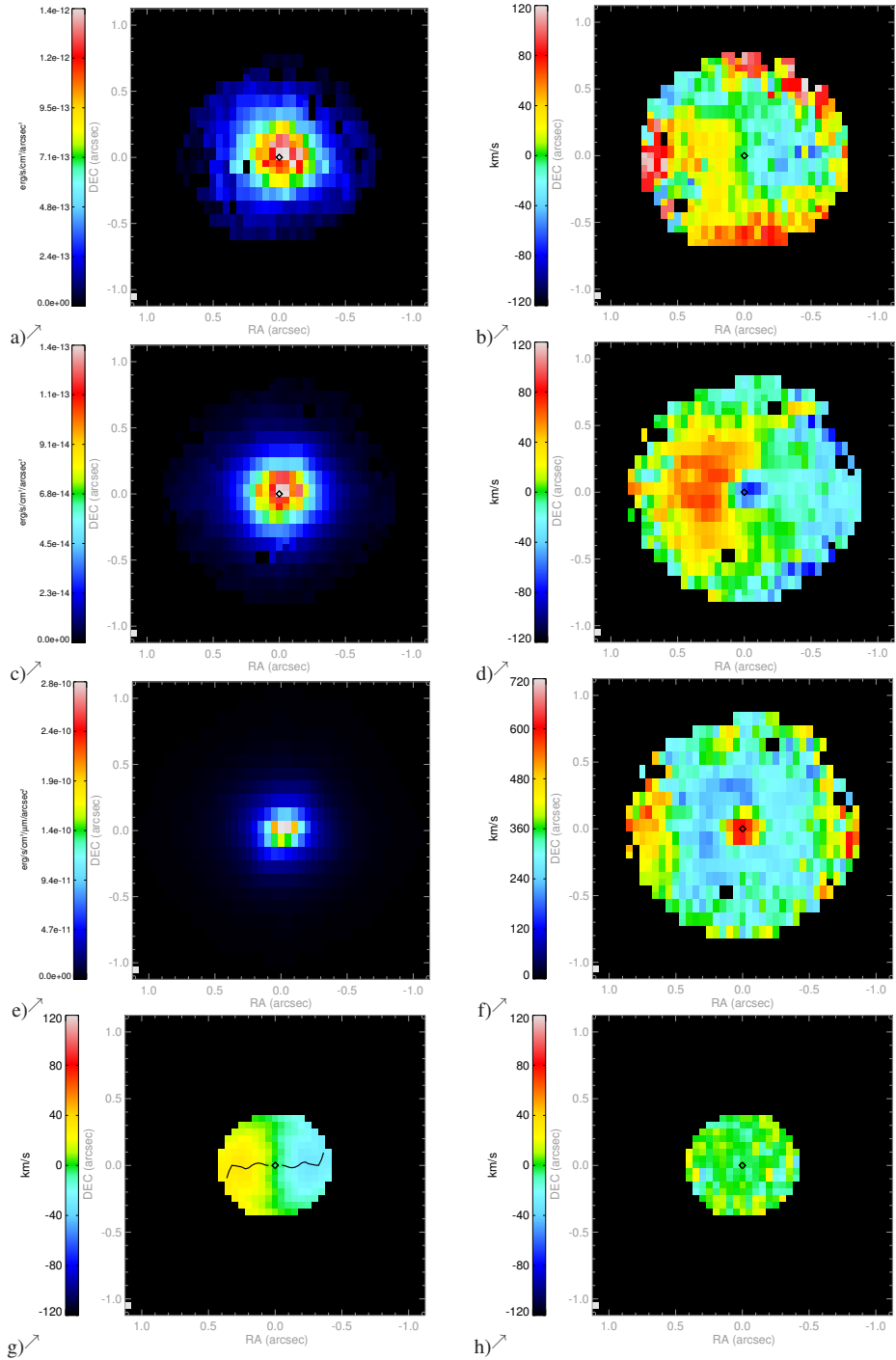


Figure 5.4 – IRAS 05189-2524 gas rotation curve of H<sub>2</sub>.



**Figure 5.5** – IRAS 05189-2524 ( $f_{25}/f_{60}=0.26$ ;  $1''\approx 0.84\text{kpc}$ ); a) H<sub>2</sub> flux; b) H<sub>2</sub> velocity; c) Pa α flux; d) Pa α velocity; e) K-band continuum; f) Pa α velocity dispersion; g) velocity model of H<sub>2</sub> and h) residual map.

### 5.3.6 IRAS 09111-1007

In the spectrum of this cool ULIRG ( $f_{25}/f_{60}=0.11$ ), the high excitation [SiVI] line is detected, which denotes the presence of an AGN (Fig. 5.1, middle). The morphology of  $H_2$ , Pa  $\alpha$  and  $K$  (Fig. 5.7) is centrally concentrated in a similar way. These maps are all extended in northeast-southwest direction, aligned with the axis of rotation (velocity field, Fig. 5.7b,d), although the  $H_2$  extension and rotation axis seems to be tilted with a slightly different angle. The velocity dispersion map of Pa  $\alpha$  (f) is distorted and peaks north, with a dip directly to the south-west of the NIR/kinematic centre. The velocity map of Pa  $\alpha$  is used for modelling, but the seemingly symmetric deviations of the rotation axis are not modelled properly, leaving higher residuals on the edges (g) and (h).

The velocity field of Pa  $\alpha$  is not symmetric, as can be seen in the residual map of the fit. It should also be noted that the minimum in the blueshifted part does not have a clear corresponding maximum in the redshifted part in the observed Pa  $\alpha$  velocity map. These details should be kept in mind when inspecting the fit to the rotation curve, which appears to be satisfactory. The inclination used was  $38^\circ$ . The curve was fit with bulge and a disk components, with resulting values  $R_{\text{eff}}$  of 2.3 kpc and  $M_{\text{tot}}$  of  $3.44 \cdot 10^{10} M_\odot$  for the bulge, and  $h$  of 0.5 kpc and  $\Sigma_0$  of  $4.0 \cdot 10^3 M_\odot \text{pc}^{-2}$  for the exponential disk. The outer radius  $R_{\text{out}}$  is 1.05 kpc, and  $M(R_{\text{out}})$  is  $1.34 \cdot 10^{10} M_\odot$ . The gas fraction within this radius is 0.29, and the gas mass would be  $M = 3.6 \cdot 10^9 M_\odot$ . This is in excellent agreement with the gas mass  $M = 3.1 \cdot 10^9 M_\odot$  derived for this object by Chung et al. (2009) using CO 1–0 data. The resulting value of  $M_{\text{dyn}}/L_K$  is  $0.02 M_\odot/L_{K,\odot}$ , and  $M_*/L_K$  is  $0.015 M_\odot/L_{K,\odot}$  for the stellar component. The contribution of the AGN in IRAS 09111-1007 is estimated to be negligibly small in the near-IR (Farrah et al. 2003).

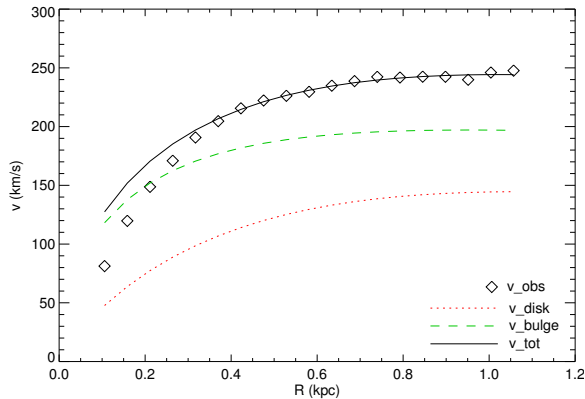
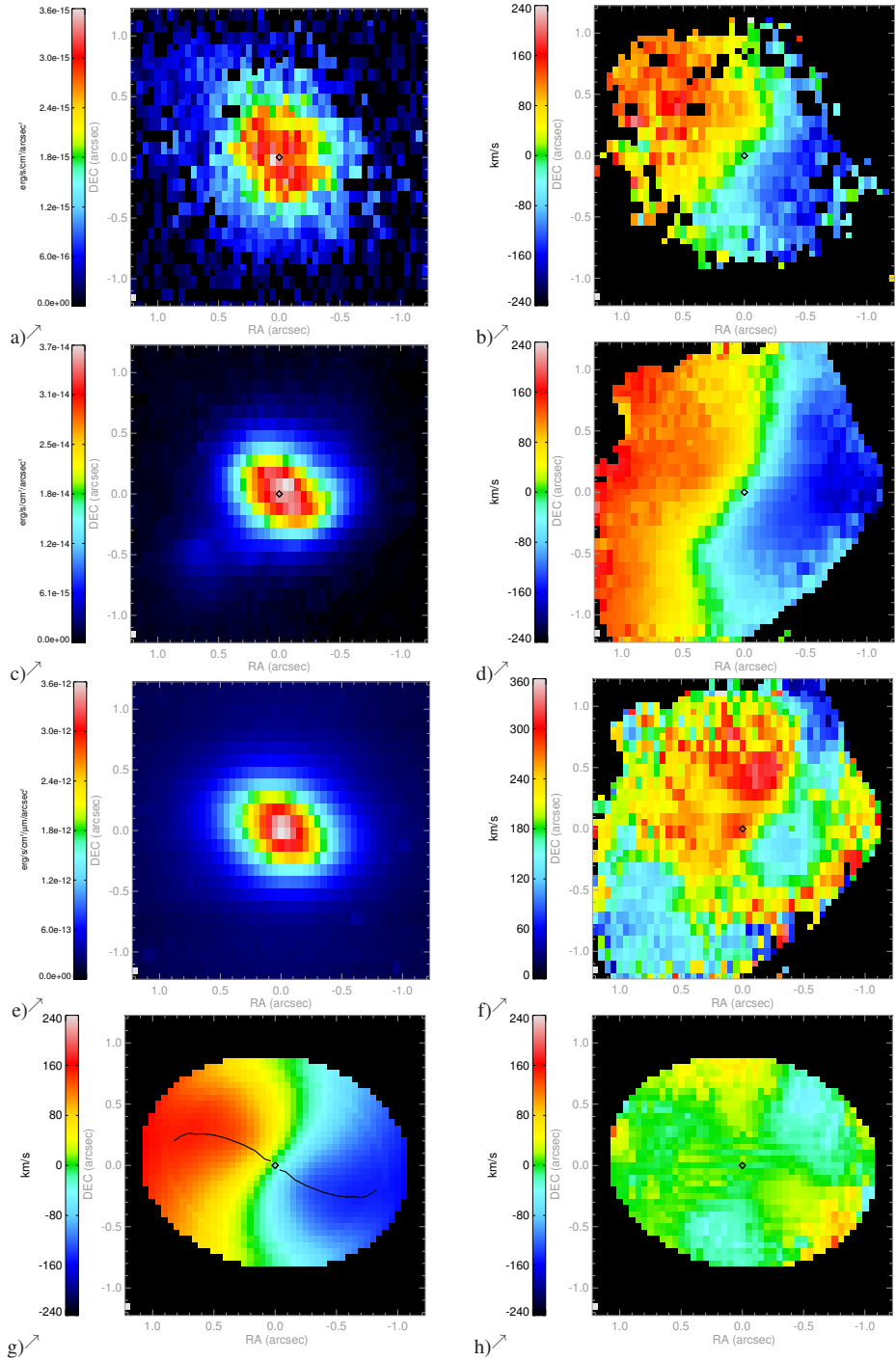


Figure 5.6 – IRAS 09111-2524 gas rotation curve of Pa  $\alpha$ .



**Figure 5.7** – IRAS 09111-1007 ( $f_{25}/f_{60}=0.11$ ;  $1'' \approx 1.07$  kpc); a) H<sub>2</sub> flux; b) H<sub>2</sub> velocity; c) Pa  $\alpha$  flux; d) Pa  $\alpha$  velocity; e) K-band continuum; f) Pa  $\alpha$  velocity dispersion; g) velocity model of Pa  $\alpha$  and h) residual map.

### 5.3.7 IRAS 17208-0014

This is the ‘coolest’ ULIRG of the sample, with  $f_{25}/f_{60}$  of 0.05, while it is also the most luminous in the infrared. The distribution and peak locations of  $H_2$ , Pa  $\alpha$  and  $K$  are all slightly different (Fig. 5.9). The velocity fields of  $H_2$  (b) and Pa  $\alpha$  (d) show minor differences, while the peak of the velocity dispersion (f) is clearly displaced to the south of the  $K$ -band peak. The Pa  $\alpha$  velocity field was used for modelling (g), and the kinematic centre had to be shifted to the south-east with respect to the  $K$ -band peak centre. The resulting rotation curve in Fig. 5.8 shows very rapid rotation (implying a very massive system), and a declining shape beyond 0.35 kpc. A higher inclination would result in a lower derived rotation velocity, formally by at most a factor 2 (for inclination  $90^\circ$ ). However, a very edge-on orientation is ruled out by the observed morphology of both the stellar and the gaseous components, based on our data as well as high resolution CO data (Downes & Solomon 1998). So while an underestimated inclination could play a role in producing the very high derived rotation velocity, it will certainly not explain it fully, and this is certainly a rapidly rotating, and therefore massive system.

The velocity fields of  $H_2$  and Pa  $\alpha$  have slightly different features, but in both the kinematic centre seems to be shifted to the south, with respect to the  $K$ -band peak. The redshifted and blueshifted peaks in the Pa  $\alpha$  velocity map are not exactly symmetric, which is seen in the residual map, though the residuals are not high compared to the measured velocities. The used inclination was  $28^\circ$ , based on the CO interferometry of Downes & Solomon (1998). The resulting rotation curve declines after the turnover-point at 0.35 kpc. If only fitted with a Hernquist potential, the effective radius needed to establish this shape would be very small, of the order of 0.05 kpc. The gas component is essential to make a reliable fit. In this case, the mass of the gas disk could be constrained with CO-data from Downes & Solomon (1998). The scale length  $h=0.46$  kpc was derived from the gas mass difference between their observed radii of  $R_{\text{out}}=1.5$  kpc and  $R_{\text{in}}=0.54$  kpc and the mass surface density  $\Sigma_0 = 5.5 \cdot 10^3 M_\odot \text{pc}^{-2}$  was calculated accordingly. The spheroid component was then fitted with  $R_{\text{eff}}$  of 0.54 kpc and  $M_{\text{tot}}$  of  $6.35 \cdot 10^{10} M_\odot$ . The outer radius  $R_{\text{out}}$  is 1.05 kpc, and  $M(R_{\text{out}})$  is  $1.34 \cdot 10^{10} M_\odot$ . The gas fraction within this radius is 10%.  $M_{\text{dyn}}/L_K$  is  $0.43 M_\odot/L_{K,\odot}$ , and  $M_*/L_K$  is  $0.38 M_\odot/L_{K,\odot}$ .

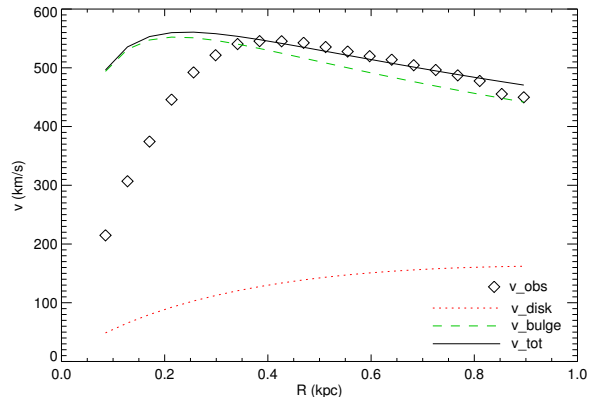
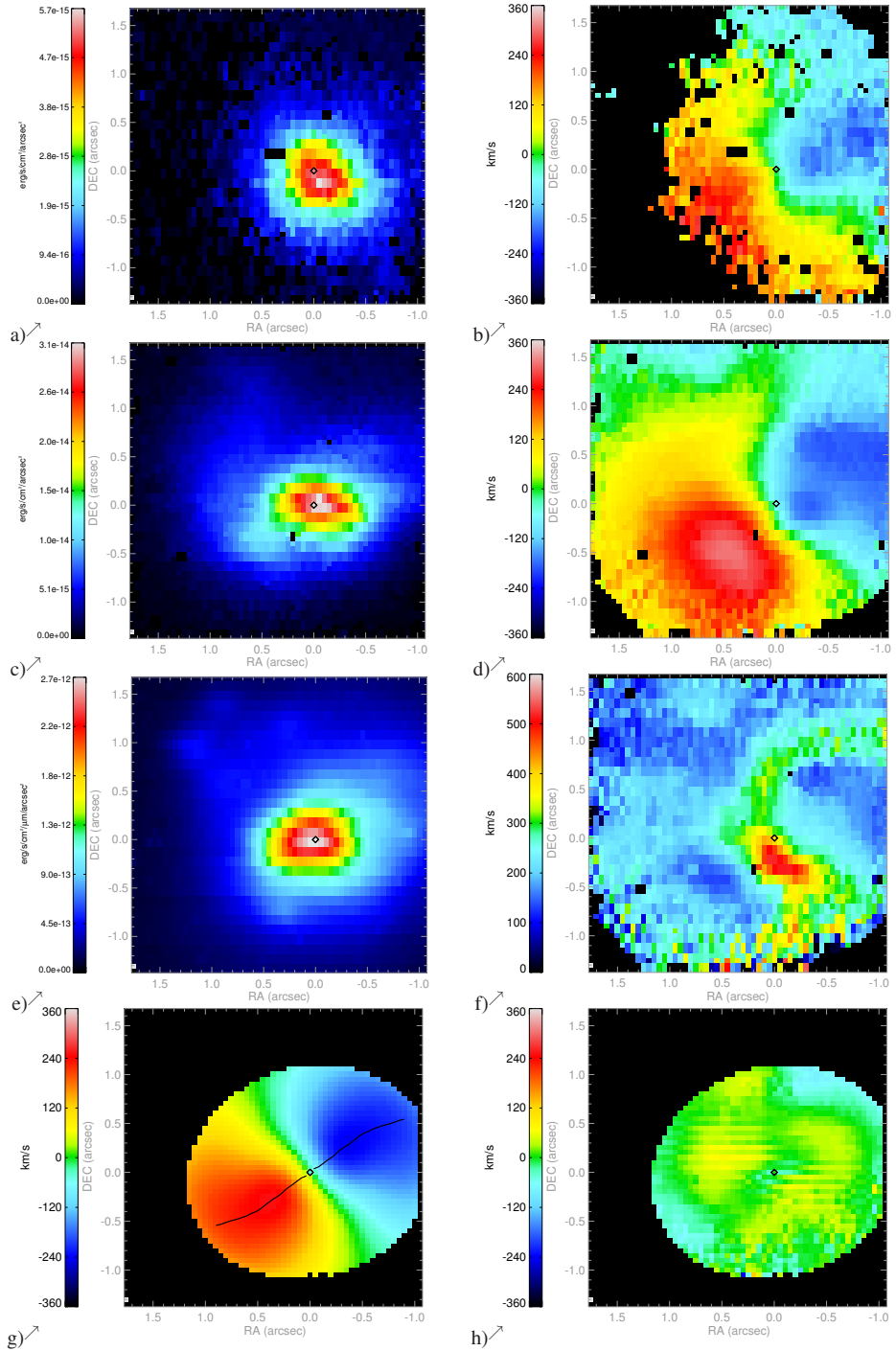


Figure 5.8 – IRAS 17208-2524 gas rotation curve of Pa  $\alpha$ .



**Figure 5.9** – IRAS 17208-0014 ( $f_{25}/f_{60}=0.05$ ;  $1'' \approx 0.86\text{kpc}$ ); a) H<sub>2</sub> flux; b) H<sub>2</sub> velocity; c) Pa  $\alpha$  flux; d) Pa  $\alpha$  velocity; e) K-band continuum; f) Pa  $\alpha$  velocity dispersion; g) velocity model of Pa  $\alpha$  and h) residual map.

### 5.3.8 IRAS 20551-4250

Regarding its infrared colours ( $f_{25}/f_{60}=0.15$ ), this is a moderately warm ULIRG. The source is quite compact in  $H_2$ , Pa  $\alpha$  and  $K$  (Fig. 5.11). Only the relatively faint emission shows some structure, a tail towards the south-east in  $H_2$ , and extension to the north and west in Pa  $\alpha$ . The velocity fields of  $H_2$  (b) and Pa  $\alpha$  (d) show little rotation, and although it seems regular in  $H_2$ , it is more likely that this velocity field has the same distortions as the Pa  $\alpha$ . The velocity dispersion (f) is very distorted with dips and peaks, a dip on the NIR centre location. An attempt has been made to make a model of the Pa  $\alpha$  velocity field (g,h), but it only models part of the field and it is not clear that the assumed rotation axis (with the highest gradient in the complex Pa  $\alpha$  velocity field) should be correct.

As mentioned above, the velocity field is not regular though part of it seems to show rotation about the centre (centres of  $H_2$ , Pa  $\alpha$  and  $K$  do coincide, however). Also, the fitted region does not extend to the location where the minimum (blueshifted) velocity is reached (which does not have a maximum/redshifted counterpart). The part that *is* fitted, does not have large values in the residual map (h), but a hint that the minimum velocity is not included can be seen in the southwest. The inclination used was  $36^\circ$ . A combined fit to the rotation curve (Fig. 5.10) was made with a spheroid component with ( $R_{\text{eff}}=1.5$  kpc and  $M_{\text{tot}}$  of  $5.75 \cdot 10^9 M_\odot$ ) and a disk component with ( $h=0.35$  kpc and  $\Sigma_0 = 9.0 \cdot 10^2 M_\odot \text{pc}^{-2}$ ). The total dynamical mass within 1.5 kpc is then  $2.52 \cdot 10^9 M_\odot$ , with a gas fraction of 20%. The value of  $M_{\text{dyn}}/L_K$  is  $0.05 M_\odot/L_{K,\odot}$ , and  $M_*/L_K$  is  $0.04 M_\odot/L_{K,\odot}$ .

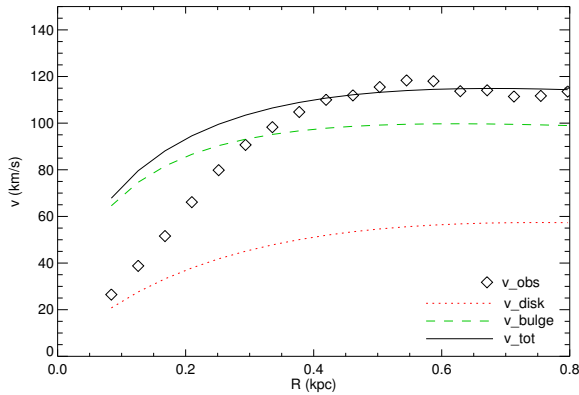
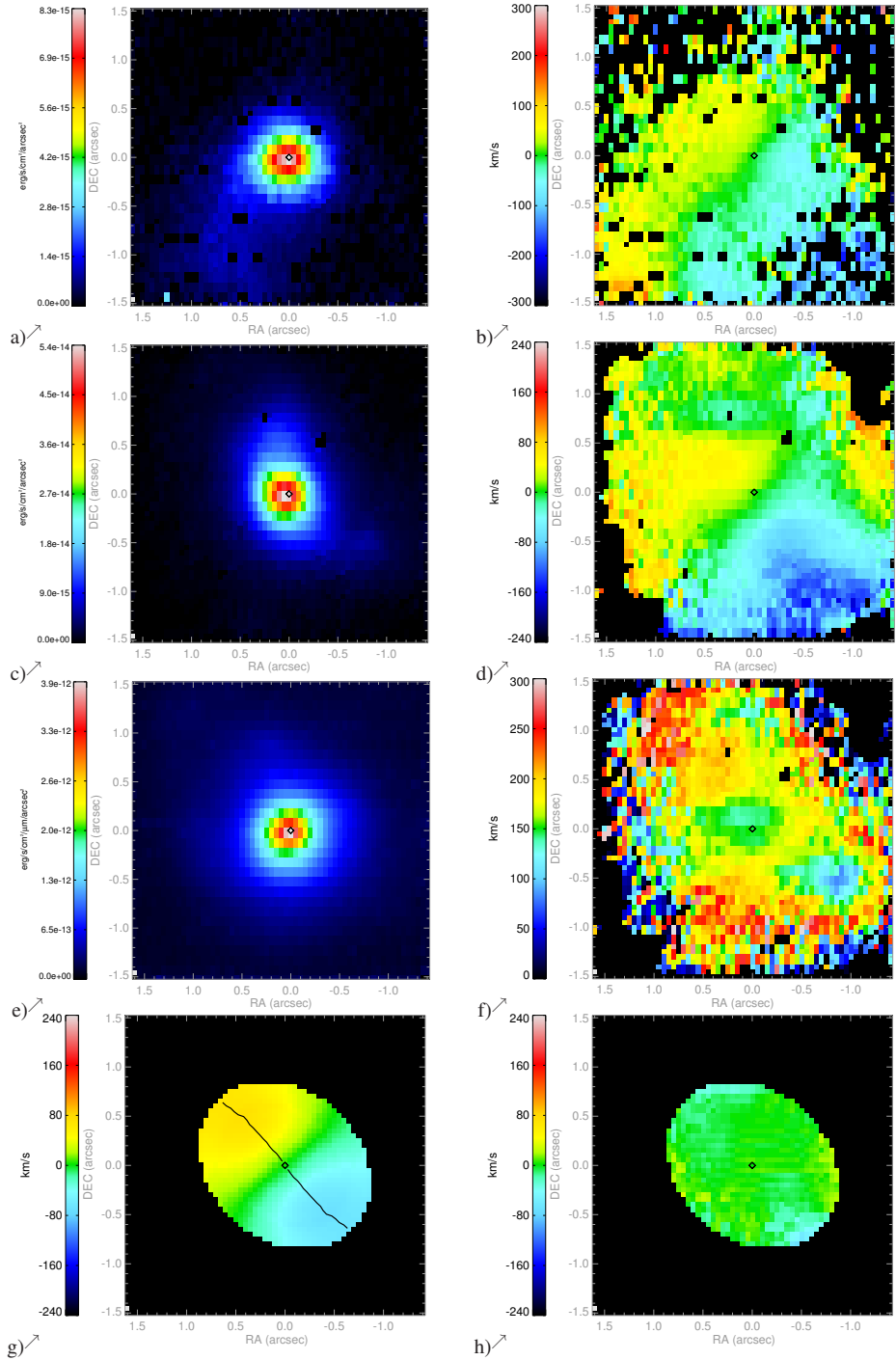


Figure 5.10 – IRAS 20551-4250 gas rotation curve of Pa  $\alpha$ .



**Figure 5.11** – IRAS 20551-4250 ( $t_{25}/t_{60}=0.15$ ;  $1''\approx 0.86\text{kpc}$ ); a) H<sub>2</sub> flux; b) H<sub>2</sub> velocity; c) Pa α flux; d) Pa α velocity; e) K-band continuum; f) Pa α velocity dispersion; g) velocity model of Pa α and h) residual map.

**Table 5.3** – Mass and luminosity within the SINFONI-field of view.

Name	$R_{\text{out}}$ (kpc)	$M_{\text{gas}}$	$M_*$	$M_{\text{dyn}}$	$M_{\text{gas}}/M_{\text{dyn}}$	$L_K$	$M_{\text{dyn}}/L_K$	$M_*/L_K$	$M_{\text{dyn}}^{(*)}$	$M_*/L_K^{(*)}$
(1)	(2)	(3)	(4)	(5)	(6)	(7)	(8)	(9)	(10)	(11)
		$(10^{10} M_{\odot})$	$(10^{10} M_{\odot})$			$(10^{10} L_{K,\odot})$	$\left(\frac{M_{\odot}}{L_{K,\odot}}\right)$		$(10^{10} M_{\odot})$	$\left(\frac{M_{\odot}}{L_{K,\odot}}\right)$
IRAS 01388-4618	2.4	1.0	1.2	2.2	0.46	108	0.02	0.01	$6.0 \pm 1.0$	$0.03 \pm 0.01$
IRAS F05189-2524	0.34	-	0.052	0.052	-	$17.5^a$	0.003	0.003	$0.87 \pm 0.25$	$0.05 \pm 0.02$
IRAS F09111-1007	1.1	0.4	0.95	1.3	0.29	63.6	0.02	0.015	$1.8 \pm 0.7$	$0.02 \pm 0.01$
IRAS F17208-0014	1.0	0.47	4.2	4.7	0.10	11.0	0.43	0.38	$3.3 \pm 1.6$	$0.27 \pm 0.16$
IRAS F20551-4250	0.9	0.050	0.20	0.25	0.20	5.62	0.05	0.04	$1.9 \pm 1.4$	$0.27 \pm 0.21$
Arp 220	0.6	0.50	0.70	1.19	0.42	9.01	0.13	0.08	$1.2 \pm 0.4$	$0.05 \pm 0.02$

(\*) Note: errors for the derived masses are not stated here, but the effect of the uncertainties are discussed in the text instead (Sections 5.3.3 and 5.4.2). Columns: (2)  $R_{\text{out}}$  is the major axis length of the outer ellipse of the Kinemetry-fit within the SINFONI field of view. All quantities of  $M_{\text{dyn}}$ ,  $L_K$  and  $M/L_K$  in this table are calculated within  $R_{\text{out}}$ . (3) Mass of the gas (exponential disk) component within  $R_{\text{out}}$ . (4) Mass of the stellar (bulge) component within  $R_{\text{out}}$ . (5) Total dynamic mass (gas+stars) within  $R_{\text{out}}$ . (6) Gas mass fraction. (7)  $L_K$  is the  $K$ -band luminosity within  $R_{\text{out}}$ , corrected for extinction, expressed in solar  $K$ -band luminosities ( $M_{K,\odot}=3.28$ ). The error in  $L_K$  is  $\sim 20\%$ , based on the error in  $L_K$ (uncorr) and the extinction correction. (8)  $M_{\text{dyn}}/L_K$  within  $R_{\text{out}}$ . (9)  $M_*/L_K$  within  $R_{\text{out}}$ , using only  $M_b$ . (10), (11)  $M_{\text{dyn}}$  and  $M_*/L_K$  from stellar kinematics (Chapter 4) in the same the same region, for comparison with columns (5) and (9), respectively.

<sup>a</sup> For  $L_K$ , a component of 55% has been subtracted for the AGN. The error estimate in  $L_K$  of IRAS 05189-2524 is 30%.

## 5.4 Discussion

### 5.4.1 Rotation curve fitting and the role of the effective radius, $R_{\text{eff}}$

The effective radius is commonly defined as the radius within which half of the light is contained. However, using this definition the effective radius is known to vary with the wavelength of observation (e.g., Temi et al. 2008). This is also discussed in Chapter 4 (Sect. 4.3.1 and 4.4.1), where the effective radius is important in the calculation of the dynamical mass from stellar kinematics: the total mass scales linearly with  $R_{\text{eff}}$ . When fitting the rotation curve from gas kinematics, the effective radius is one of the free parameters in the Hernquist potential that constrains the bulge component. We consider this a mass-based effective radius: the mass-to-light ratio is assumed constant, and  $R_{\text{eff}}$  should in practise be equal to the half-mass radius. The effective radius of the bulge fit is important for the shape of the rotation curve, especially in the outer parts. A declining or flat rotation curve needs a bulge with a small enough effective radius; the scale-length  $h$  only has a limited effect and the curve of a purely exponential disk potential only rises. In general, the relative importance of bulge and disk is degenerate, but we try to put constraints on the gas disk e.g. from detailed CO gas measurements, such as in Arp 220 and IRAS 17208-0014. Because literature values of  $R_{\text{eff}}$  from  $K$ -band or  $H$ -band imaging can vary greatly between  $H$ -band and  $K$ -band, and between different observations in the same band as well (compare e.g., Dasyra et al. 2006, Genzel et al. 2001, Scoville et al. 2000, Veilleux et al. 1999), it is difficult to state what is the effect of our approach, although most of the mass-based effective radii are smaller than their  $K$ -band or  $H$ -band derived counterparts. It is no surprise that the effective radius of the compact source IRAS 05189-2524 is small (0.35 kpc), while the value of IRAS 17208-0014 (0.54 kpc) is much more surprising, compared to 1.4 kpc from Genzel et al. (2001) and 2.6 kpc from Scoville et al. (2000). However, for this target the possible range of  $R_{\text{eff}}$  was very small because of the declining shape of the, in this case, well defined rotation curve and the gas mass constrained by CO-observations of Downes & Solomon (1998). The value of IRAS 20551-4250 (1.5 kpc) is smaller than the 2.1 kpc determined by both Genzel et al. (2001) and Rothberg & Fischer (2010), but the observed velocity field shows structure that could not be incorporated in the Kinemetry fit and the rotation curve can not be considered reliable. As mentioned before, high extinction values ( $A_K \sim 5$ ,  $A_V \sim 50$  for a foreground screen model, or higher) can be expected in the central nuclear regions of ULIRGs which can cause the effective radius to appear larger, even in the  $K$ -band where its value is minimum (Temi et al. 2008). Another cause that can affect the observed effective radius is incomplete relaxation, i.e. the stellar components of the objects that are approximated with bulge models, are in fact not spherically symmetric. This affects our approach as well as the fitting of light-curves.

### 5.4.2 Mass from gas dynamics vs. mass from stellar dynamics

Dynamical masses were also derived from stellar kinematics ( $\sigma_*$ ,  $v_*$ ) from the same dataset, as described in Chapter 4. The derived masses and mass-to-light ratios for the same regions

are stated in columns (10) and (11) of table 5.3, respectively, which can be compared to columns (5) and (9) directly. Except for IRAS 17208-0014, all mass-to-light ratios (masses) derived from the gas kinematics in this work are smaller than those from stellar dynamics. As discussed in Sect. 5.3.3, a major factor in the error of the rotation curve and the derived mass is the inclination. The inclination affects both the mass from gas dynamics and from stellar dynamics, but in different ways: in the stellar dynamics the velocity dispersion  $\sigma_*$  is the dominant factor. Although we do not give an error for the inclination, we did define a plausible inclination-range as given in Table 5.2. We tested if it is possible to match the masses from stellar and gas kinematics within the limiting values of the inclination (assuming in all cases the same inclination for the stellar and gaseous components). This is indeed the case for 3 of the ULIRGs: IRAS 09111-1007, IRAS 17208-0014 and Arp 220, which is also reflected by the fact that the masses from gas dynamics are already within the error margins of the masses from stellar dynamics. For the discrepancy in masses of the other objects, we require different explanations.

In IRAS 20551-4250, a significant part of the gas velocity field (Fig. 5.11b,d) is irregular and disturbed, and even in the direct vicinity of the nucleus where it does show rotation, the minimum values do not have corresponding maximum counterparts. This causes the Kinemetry-fit to stop at a small radius, resulting in a model velocity field that does not represent the actual velocity field well. The stellar kinematics, on the other hand, were derived with good accuracy but even with high error margins they do not come close to the gas dynamics. From this we conclude that the mass from stellar kinematics is the best estimate, whereas the mass from gas dynamics is unacceptably unreliable, since the gas velocity field is not sufficiently accurately represented by our tilted ring model.

In IRAS 05189-2524, the mass difference is quite large, a factor of 17. An interesting finding is that the stars rotate faster than the  $H_2$  gas. The stellar kinematics are only measured for a radius of  $\sim 0.4''$  and outwards, while the gas velocity (model) is only derived within a similar radius (Fig. 5.5g), but there is an overlap between the measured velocity fields and furthermore the stellar velocities do not change much towards the outer regions. We conclude that, even though the position angles of the stellar and gas velocity fields are roughly aligned, the kinematics are decoupled, i.e., they have different inclinations, which is not an unexpected observation in an advanced merger remnant. In this case, the gas would be more face-on than the stars.

The mass difference in IRAS 01388-4618 is not very large, a factor of 2.7 which can be brought down to a factor of 1.8 within the error and inclination limits. For this object we did not have 2-d stellar kinematics because of the large redshift, and we used the values for ( $v_*$ ,  $\sigma_*$ ) of Dasyra et al. (2006) that were derived from slit data. We note that their slit position angle of  $55^\circ$  does match that of the kinematic major axis of the gas in our data ( $56^\circ$ , table 5.2), so that the comparison is valid. We have already noted the extended nature of the Pa  $\alpha$  disk, including a prominent feature that is probably a spiral arm. However, the (total) dynamical mass from the gas kinematics will not be affected too much and we consider this mass to be the more reliable. The value of  $M_*/L_K$  is then likely to lie between  $0.01-0.02 M_\odot/L_{K,\odot}$ , given that the disk likely contains a stellar component as well.

With the stellar and gas kinematic data in hand we can ask the question which one pro-

vides a better dynamical mass tracer. Even based on our limited sample, we have to conclude that the stellar kinematics provide a better measurement. In both measurements the inclination of the rotating system (whether stars or gas) is the dominant source of uncertainty, but for the stars its importance is offset by the effects of the stellar velocity dispersion in these dynamically hot systems. However, even if the inclination could be reliably measured (which is possible using sufficiently accurate and high S/N data), the stellar dynamics still performs better, since in many objects the gas does not appear to have settled in a simple dynamical configuration that can be adequately modelled by a set of tilted rings. In contrast, the stellar components seem to be, within the accuracy of our measurements, dynamically fairly relaxed. This is a somewhat surprising result, since the gas components are dissipative, leading to a rapid merging and loss of memory of its former dynamical properties, while the stellar component would merge on longer timescales due to dynamical friction. Apparently a process of rapid relaxation gives rise to dynamically well-behaved stellar cores, supported by rotation and random motions. It is possible that deeper measurements would reveal traces of unrelaxed dynamics, but at the S/N ratio of our data such traces are not found.

### 5.4.3 ULIRG evolution: starburst ages and mass fractions

Despite the differences mentioned in the section above, the fact that there is no trend of  $M/L_K$  with  $f_{25}/f_{60}$  is a confirmation of the result from stellar dynamics (Chapter 4). The ages derived from a starburst model for the most plausible value of  $M_*/L_K$  range from  $\sim 10$  Myr for IRAS 01388-4618, IRAS 09111-1007 and probably also for IRAS 05189-2524 to  $\sim 15$  Myr for Arp 220 and  $\sim 100$  Myr for IRAS 17208-0014 and IRAS 20551-4250 (see Chapter 4, section 4.3.1 for a description of the model). These values are consistent with those in Chapter 4, and likewise we confirm the conclusion that these merging galaxies undergo several burst events: one at their first encounter and again when they finally merge, while  $M/L_K$  only indicates the age of the most recent merging event.

The gas fractions derived from the rotation curve fit, within the observed radius  $R_{\text{out}}$ , range from 10% to 50% (no estimate for IRAS 05189-2524). This range is in agreement with the values found by e.g. Tacconi et al. (2002). The gas fraction of 50% found in IRAS 01388-4618 may be somewhat overestimated (see Sect. 5.4.2), but even with this 50% included, the overall gas component is not dominant in these objects. In the possible evolutionary path from ULIRGs to ellipticals, the gas is consumed and the gas fraction is expected to decrease with evolutionary state. No such (anti)correlation is found between infrared colour  $f_{25}/f_{60}$  and gas fraction, but because of the limited size of our sample we do not attach significance to this result.

### 5.4.4 ULIRG evolution: the fundamental plane

With our data, it is possible to pinpoint the location of ULIRGs with respect to the Fundamental Plane to find out if and in what way it is related to the location of (giant) elliptical galaxies and bulges.

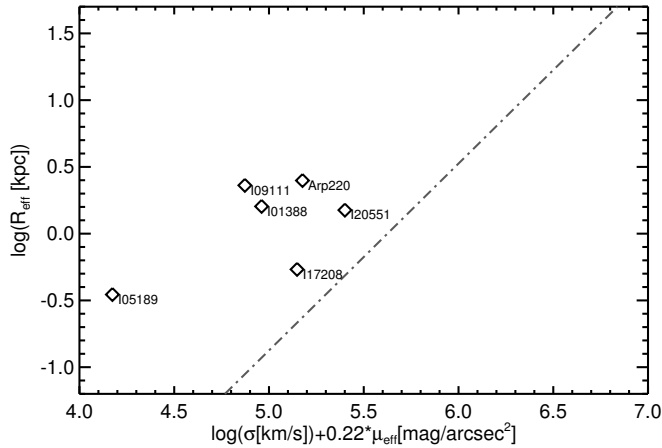


**Figure 5.12** – Location of the sample ULIRGs with respect to fundamental plane. The dot-dashed line indicates the location of a projection of the fundamental plane of hot galaxies: it is the best-fit slope from  $K$ -band studies of Mobasher et al. (1999) and Pahre (1999):  $\log r_{\text{eff}} = 1.4[\log \sigma + 0.22\mu_{\text{eff}}(K)] + \text{const}$ , as fitted to the data of Genzel et al. (2001) and Tacconi et al. (2002).

We use the effective radius as derived from the bulge-fit, which should better match the properties of elliptical galaxies, because these do not suffer from the high extinction as is supposed to be the case in ULIRGs, see also Sect. 5.4.1. Next, we calculated  $\mu_{\text{eff}}$ , the extinction corrected value of the  $K$ -band surface brightness within  $R_{\text{eff}}$ . When  $R_{\text{eff}}$  was outside of our field of view,  $\mu_{\text{eff}}$  was determined by extrapolation, assuming a Hernquist bulge for the light profile (and assuming constant M/L):

$$L_K(R_{\text{eff}}) = \frac{(R_{\text{max}} + a)^2}{(R_{\text{eff}} + a)^2} \left( \frac{R_{\text{eff}}}{R_{\text{max}}} \right) \cdot L(R_{\text{max}}),$$

which is derived directly from the relation  $M(r) = M_{\text{tot}} \frac{r^2}{(r+a)^2}$  and  $a = R_{\text{eff}}/\sqrt{2}$  from Hernquist (1990). The stellar velocity dispersion ( $\sigma_*$ ) was derived in Chapter 4. Fig. 5.12 shows the ULIRGs in a specific projection of the fundamental plane with the least scatter as in Genzel et al. (2001), Tacconi et al. (2002), Dasyra et al. (2006). Our ULIRGs are all located to the left of this particular projection of the fundamental plane, which can be explained entirely by the fact that they all have lower  $K$ -band M/L ratios than quiescent ellipticals, and is in agreement with earlier work (e.g., Genzel et al. 2001, Tacconi et al. 2002, Dasyra et al. 2006). Passive evolution (with no evolution in structural properties) would move these objects to the right where they eventually would lie on the fundamental plane. They would however not lie in the region of giant ellipticals (which have larger effective radii), but in the region of intermediate mass (and luminosity) ellipticals, and this conclusion is even stronger than the conclusion from earlier work (Genzel et al. 2001, Tacconi et al. 2002, Dasyra et al. 2006), due to the somewhat smaller  $R_{\text{eff}}$  found for most of our targets. Therefore we find that ULIRGs

do not evolve into massive giant ellipticals but into intermediate mass and luminosity ellipticals, unless further *dynamical* evolution would lead to higher values of  $R_{\text{eff}}$ . This is not totally out of the question, given the fact that many of these objects are still in the process of merging, and complex configurations were found in particular in the gas dynamics. Detailed simulations of gas-rich star-forming mergers are needed to address this issue in more detail.

## 5.5 Conclusions

We have observed the central regions of 6 ultraluminous infrared galaxies with high resolution near infrared integral field spectroscopy. We derived the velocity fields from Pa  $\alpha$  and H<sub>2</sub> and modelled the rotation curve with a stellar and a gas component, and derived  $K$ -band mass-to-light ratios within the field of view. These were compared with mass-to-light ratios from stellar kinematics from the same dataset. We draw the following conclusions.

1. Stellar mass-to light ratios are generally smaller as derived from gas kinematics as compared to those from stellar kinematics, but they are consistent taking into account the uncertainties of the inclination, which forms the dominant source of uncertainty in the derived parameters.
2. There is no trend of  $M/L_K$  with infrared colour  $f_{25}/f_{60}$ , which is confirmed by the stellar kinematics.
3. The effective radius is an important factor in the mass-determinations both in gas and stellar kinematics.  $R_{\text{eff}}$  is generally smaller when derived from the bulge potential than when derived from the  $K$ -band lightcurve. We ascribe this to high extinction in the nuclear region.
4. We confirm earlier findings that, in the fundamental plane, ULIRGs are not evolving into giant ellipticals. The difference in effective radius with giant ellipticals is a factor of 3 in our study, which is beyond the error margins and even higher than previous studies.
5. We find that the gas velocity fields are considerably affected by bulk motions and asymmetries, most likely resulting from the merger nature of our targets. These motions cannot be modelled using tilted ring models, and this limits the power of gas dynamics for analysing the gravitational dynamics. The stellar dynamics seem comparably well-behaved and probably provide a cleaner measurement of the dynamical masses of these systems.

## References

- Bonnet, H., Abuter, R., Baker, A., et al. 2004, *The Messenger*, 117, 17  
Cappellari, M., Neumayer, N., Reunanen, J., et al. 2009, *MNRAS*, 394, 660  
Chung, A., Narayanan, G., Yun, M. S., Heyer, M., & Erickson, N. R. 2009, *AJ*, 138, 858

- Dasyra, K. M., Tacconi, L. J., Davies, R. I., et al. 2006, *ApJ*, 651, 835
- Downes, D. & Solomon, P. M. 1998, *ApJ*, 507, 615
- Eisenhauer, F., Abuter, R., Bickert, K., et al. 2003, in *Proceedings of the SPIE, Vol. 4841, Instrument Design and Performance for Optical/Infrared Ground-based Telescopes.*, ed. M. Iye & A. F. M. Moorwood, 1548–1561
- Elmegreen, B. 1994, in *Violent Star Formation from 30 Dor to QSOs*, ed. T. G.
- Farrah, D., Afonso, J., Efstathiou, A., et al. 2003, *MNRAS*, 343, 585
- Ferrarese, L. & Merritt, D. 2000, *ApJ*, 539, L9
- Gebhardt, K., Bender, R., Bower, G., et al. 2000, *ApJ*, 539, L13
- Genzel, R., Tacconi, L. J., Rigopoulou, D., Lutz, D., & Tecza, M. 2001, *ApJ*, 563, 527
- Goldader, J. D., Joseph, R. D., Doyon, R., & Sanders, D. B. 1995, *ApJ*, 444, 97
- Hernquist, L. 1990, *ApJ*, 356, 359
- Krajnović, D., Cappellari, M., de Zeeuw, P. T., & Copin, Y. 2006, *MNRAS*, 366, 787
- Magorrian, J., Tremaine, S., Richstone, D., et al. 1998, *AJ*, 115, 2285
- Mobasher, B., Guzman, R., Aragon-Salamanca, A., & Zepf, S. 1999, *MNRAS*, 304, 225
- Neumayer, N., Cappellari, M., Reunanen, J., et al. 2007, *ApJ*, 671, 1329
- Pahre, M. A. 1999, *ApJS*, 124, 127
- Rothberg, B. & Fischer, J. 2010, *ApJ*, 712, 318
- Sanders, D. B., Mazzarella, J. M., Kim, D.-C., Surace, J. A., & Soifer, B. T. 2003, *AJ*, 126, 1607
- Sanders, D. B., Soifer, B. T., Elias, J. H., et al. 1988, *ApJ*, 325, 74
- Scoville, N. Z., Evans, A. S., Thompson, R., et al. 2000, *AJ*, 119, 991
- Tacconi, L. J., Genzel, R., Lutz, D., et al. 2002, *ApJ*, 580, 73
- Temi, P., Brighenti, F., & Mathews, W. G. 2008, *ApJ*, 672, 244
- Veilleux, S., Kim, D.-C., & Sanders, D. B. 1999, *ApJ*, 522, 113



